nature communications

Article

https://doi.org/10.1038/s41467-024-54802-0

Maximizing light-to-heat conversion of $Ti_3C_2T_x$ MXene metamaterials with wrinkled surfaces for artificial actuators

Received: 17 March 2024

Accepted: 20 November 2024

Published online: 03 December 2024

Check for updates

Hwansoo Shin[1,2], Woojae Jeong[1,2] & Tae Hee Han[1,2,3]

MXene, a promising photothermal nanomaterial, faces challenges due to densely stacked nanosheets with high refractive index (RI). To maximize photothermal performance, MXene metamaterials (m-MXenes) are developed with a superlattice with alternating MXene and organic layers, reducing RI and inducing multiple light reflections. This approach increases light absorption, inducing 90% photothermal conversion efficiency. The m-MXene is coated onto liquid crystal elastomer (LCE) fibers, as actuating platforms via a dip-coating (m-MXene/aLCE fiber), exhibiting excellent light-driven actuating owing to the synergetic effect of the patterned m-MXene laysers by structural deformation. The m-MXene/aLCE fibers lift ~6,900 times their weight and exhibit a work density 6 times higher than that of human skeletal muscle. It is applied to artificial muscles, grippers, and a bistable structure (a shooting device, and switchable gripper). Our study offers an effective strategy to enhance light absorption in 2D nanomaterials and contributes to advancements in photothermal technologies in various fields.

The photothermal effect is a primitive and effective means of light-to-heat energy conversion through the absorption of several photons in the light, as well as a potential strategy for applications such as solar water desalination, energy harvesting, solar photothermal electrodes, photothermal catalysis, biomedicine, sensors, smart window, and light-driven actuators[1,2]. Notably, light is a safe, clean, remote, and readily controllable energy source whose features such as intensity, wavelength, specific size, and exposure time can be modulated[3,4]. Such photothermal conversions can be exhibited by various nanomaterials, such as metal nanomaterials, carbon nanomaterials, semiconductors, polymers, transition metal dichalcogenides, and transition metal carbides/nitrides (MXenes)[5–7].

Among them, MXenes, typical 2D nanomaterials, are an exceptional candidate for light-to-heat conversion. Highly metallic $Ti_3C_2T_x$ MXene exhibits a perfect internal photothermal efficiency (~100%) through the plasmonic effect[8]. $Ti_3C_2T_x$ MXene with excellent photothermal performance and low emissivity has been studied for broad applications[9]. To expand the potential of MXene as an efficient photothermal material, MXene-based composites have been extensively studied for various applications. For instance, MXene/polymer nanocomposites have been applied in phase-change materials, bimodal photothermal/chemotherapy treatments, and photothermal storage systems[10–12]. The MXene surface is often modified with organic ligands, or combined with metal oxides, carbon, or metal nanomaterials to achieve superhydrophobic surfaces, enhance magnetic resonance imaging, improve biocompatibility, combine plasmonic and photothermal effects, and enhance localized surface plasmon resonance, among other multifunctionalities[13–15].

However, both $Ti_3C_2T_x$ MXene and its nanocomposites exhibit relatively low performance compared to the reported internal photothermal conversion efficiency of nearly 100%. Furthermore, the assembled $Ti_3C_2T_x$ MXene structure has demonstrated lower performance (e.g., ~20%)[16] because of the densely packed microstructure and its high refractive index (RI), resulting in high reflection on the surface of MXene[17,18]. This not only disturbs the efficient absorption of incident light but also prevents light from penetrating the inner structure. Various strategies have been studied to efficiently utilize incident light. For example, porous or hierarchical structures have been developed to

[1]Department of Organic and Nano Engineering, Hanyang University, Seoul, Republic of Korea. [2]Human-Tech Convergence Program, Hanyang University, Seoul, Republic of Korea. [3]Research Institute of Industrial Science, Hanyang University, Seoul, Republic of Korea. e-mail: than@hanyang.ac.kr

enhance light absorption[16–19]. It has been reported that the long alkyl chains in silane-modified MXene films reduce light reflection[13]. However, these strategies also affect the mechanical properties of the assembled structure, involve complex processes, and raise cost concerns for industrial applications. Additionally, they do not sufficiently demonstrate the impact on light-matter interactions. Furthermore, the reflection induced by a high intrinsic RI remains a fundamental challenge that needs to be studied in the photothermal applications of MXene.

Our study demonstrates MXene metamaterials (m-MXenes) with alternating microstructures of MXene and dielectric layers at the nanoscale, providing insights into light-matter interactions through microstructure control for efficient light absorption. A superlattice microstructure, consisting of periodic MXene nanosheets and organic layers, was developed in the self-assembled m-MXene. Repeated organic layers with a lower RI than MXene reduce the effective RI of the self-assembled structure, making the reflection of m-MXene ~2.6 times lower than that of MXene structures. The resulting m-MXene exhibited an outstanding photothermal conversion ratio (~90%) without a porous matrix. Furthermore, m-MXene can be easily coated on aligned liquid crystal elastomer (aLCE) fibers through a simple dip coating method for photothermal-based soft artificial muscles. In addition, m-MXene develops wrinkled microstructures on the surface of aLCE owing to the swelling and contraction behavior of aLCE. This arrayed surface contributes to light scattering and multiple internal reflections, resulting in the reduction of reflection and enhancement of absorption[20,21]. These assist in converting light into thermal energy. Thus, the m-MXene/aLCE fibers not only efficiently convert light to thermal energy but also show two times higher tensile strength (~6.86 MPa) than aLCE, resulting in enhanced actuating stress (~0.56 MPa) compared to MXene/aLCE (~0.21 MPa). The m-MXene/aLCE fibers are also applicable in various actuating applications, such as artificial biceps and grippers. Our study presents an effective strategy to enhance the light absorption of self-assembled 2-dimensional MXene-based nanomaterials, thereby contributing to photothermal applications, such as wearable devices and biomedical applications.

Results

Assembly of functionalized MXene sheets into metamaterials and structural analysis

The fabrication of metamaterials, composed of alternating structures of dielectric and metallic layers, has attracted significant attention for manipulating the optical properties of materials. These structured materials strongly interact with incident light, leading to a significant enhancement in light–matter absorption due to the interference effect in a geometric shape[22]. In this study, metamaterials using MXenes as highly electroconductive metallic layers and amine ligands with long alkyl chains, specifically oleylamine (OAm), as dielectric organic materials, were prepared. Specifically, amine groups are expected to exhibit strong binding energy with the MXene surface, while OAm ligands form ordered monolayers on the MXene surface[23]. MXenes were synthesized by the selective etching of Al layers from MAX phase powders. The surface of the MXene sheets was then modified with OAm ligands, resulting in OAm-MXene.

Scanning electron microscopy (SEM) analysis revealed that the obtained MXene and OAm-MXene nanosheets exhibited a similar lateral size of ~4.8 µm, implying that the chemical functionalization of MXene did not alter the morphologies of the sheets (Supplementary Fig. 1a, b). Fourier-transform infrared (FT-IR) spectroscopy revealed the presence of distinct peaks for OAm-MXene that were absent for MXene (Supplementary Fig. 1c). These peaks at 1100, 1383, 1466, 1528, 1614, 2855, 2930, and 3005 cm^{-1} correspond to ν(C–N), $\delta_s(CH_3)$, $\delta_{as}(CH_3)$, δ(N–H), ν(–C=C), ν_s(C–H), ν_{as}(C–H), and ν(=C–H), respectively. In the high-resolution X-ray photoelectron spectroscopy (XPS) spectra of MXene and OAm-MXene, the N 1*s* of OAm-MXene showed distinct peaks corresponding to Ti–N and C–N bonds at 396.8 and 400.3 eV, respectively (Supplementary Fig. 1d). In the C 1*s* spectra of OAm-MXene, a significant increase in the intensity of the C–C bonds (284.9 eV) was observed compared to that of Ti–C (281.7 eV), owing to the long alkyl chain of the amine ligands (Supplementary Fig. 1e).

To fabricate the metamaterial, OAm-MXene sheets were formed into films via vacuum-assisted filtration, resulting in the formation of an MXene metamaterial (m-MXene). For comparison, MXene films were also prepared in the same manner, and their optical properties, particularly reflection behavior, were observed (Fig. 1a). Notably, the m-MXene film was dark navy in color, whereas the MXene film was dark purple (Fig. 1b). This color distinction suggests that the m-MXene film has a higher light absorption capacity compared to MXene film, indicating a significant difference in their light-absorbing capabilities[24]. To characterize the microstructures of both MXene and m-MXene films, wide-angle X-ray scattering (WAXS) analysis was conducted with an X-ray beam incident parallel to the surfaces of the MXene and m-MXene films[25]. In both cases, anisotropic scattering patterns corresponding to the (002) peak were observed, which is an indication of the aligned MXene and OAm-MXene nanosheets within the films. The 2D WAXS patterns were further converted into 1D scattering profiles by integrating the intensities of the MXene and m-MXene films in the equatorial direction, as shown in Fig. 1c. This analysis revealed that the (002) peaks of MXene and m-MXene films appeared at ~0.51 and 0.32 $Å^{-1}$, respectively, indicating that the interlayer distance between nanosheets expanded from 12.3 to 19.5 Å owing to the presence of an organic layer at the interface between MXene nanosheets. To investigate the orientation of nanosheets, as shown in Fig. 1d, azimuthal plots were fitted, and full width at half maximum (FWHM) and Herman's orientation factors (*f*) were analyzed by extracting the intensity of (002) peaks using Eqs. (1) and (2)[26]. Both the MXene and m-MXene films displayed similar *f* values, ~0.83 and 0.84, respectively (Supplementary Fig. 1f), suggesting that the m-MXene film possesses well-ordered structures, even with organic layers between the nanosheets.

Enhanced light absorption and photothermal effect of m-MXene films

Controlling subwavelength geometry has been an effective strategy for light harvesting[27]. The m-MXene, as a metamaterial with an alternating layered structure of metallic MXene and dielectric OAm layers at the nanoscale, is one of the most suitable candidates for this purpose. Moreover, the RI difference between the MXene and OAm layers is relatively lower than that between the MXene and air layers. According to Fresnel's equation, this reduces reflectance at the interfaces within the m-MXene structure[28,29]. Additionally, the inorganic/organic interface enhances multiple interfacial reflections within the internal structure, further improving light harvesting[30]. The RI values of both MXene and m-MXene films were analyzed using ellipsometry within the wavelength range of 400–850 nm as RI plays a crucial role in influencing light reflection[29,31]. (Fig. 1e). The RI values of m-MXene were 0.8 lower than that of MXene films. To further characterize the optical properties, such as light absorbance, reflectance, and transmittance, a UV-Vis study of both the MXene and m-MXene films was conducted within the same wavelength range, as shown in Fig. 1f and Supplementary Fig. 2. While both the MXene and m-MXene films exhibited zero transmittance, the MXene films (~20%) displayed a higher reflectance than the m-MXene films (~9.5%) within the 400–850 nm range. This confirms that the structural alteration of the m-MXene films leads to a decrease in RI, as well as multiple internal reflections owing to the expanded layered structure[32,33], resulting in the enhancement of light absorption by maximizing the light-harvesting performance of the MXene nanosheets.

The improved light-harvesting ability of the m-MXene films directly translated into enhanced light-to-heat conversion efficiency.

https://doi.org/10.1038/s41467-024-54802-0

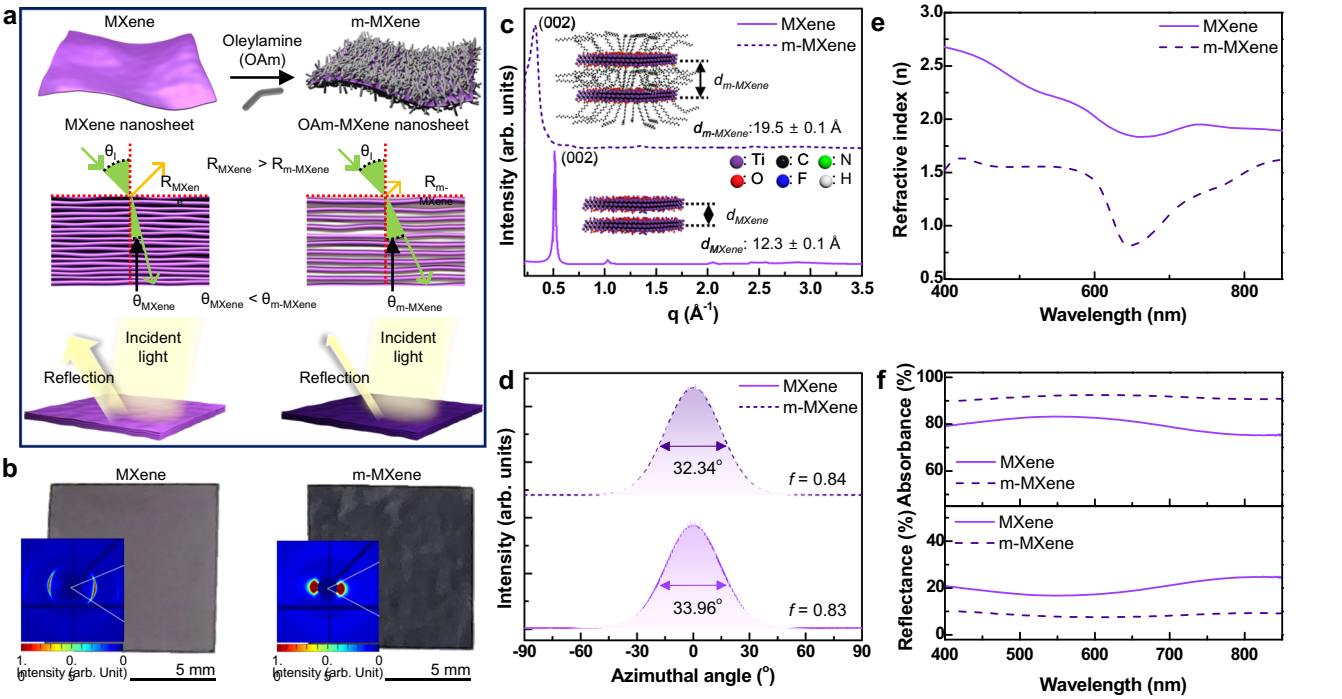

Fig. 1 | Structural and optical analysis of MXene metamaterials (m-MXene). **a** Schematic of surface modification, refractive behavior, superlattice structure, and light reflection of MXene and m-MXene film. The R and θ represent the reflectance and angle. **b** Optical images and WAXS 2D patterns of MXene and m-MXene films, **c** q plots, **d** azimuthal plots, **e** refractive index (RI), and **f** reflectance and absorbance of MXene and m-MXene films. In azimuthal plots, the shading represents the raw data, while the solid and dotted lines indicate the smoothed data.

When exposed to an incident of NIR laser (808 nm) with varying power densities (0.12, 0.33, 0.43, 0.61, and 0.71 W cm^{-2}), the surface temperatures of both MXene and m-MXene films were measured, as obtained by an IR camera (Fig. 2a, b). The results show that the m-MXene films consistently achieve higher temperatures than the MXene films at all power densities. The surface temperatures of the m-MXene films were ~1.7 times higher than those of the MXene films at all power densities (Fig. 2c, d). Interestingly, the heating rate of m-MXene films (211.0 K s^{-1}) was 1.6-fold higher than that of MXene films (155.2 K s^{-1}) on average to reach the equilibrium temperature. This stems from the excellent light-harvesting performance of the m-MXene films. Photothermal efficiencies (η_{PT}) of MXene and m-MXene films were calculated using Eqs. (3) and (4) for 0.71 W cm^{-2} power density (Supplementary Fig. 3a, b)[34]. Notably, the m-MXene films showed an outstanding efficiency of close to 90%, which was 2.3 times higher than that of the MXene films (38%). As shown in Fig. 2e, the exceptional performance of the m-MXene films highlights the significant impact of the superlattice structure on enhancing light-to-heat conversion, outperforming other MXene, metals, ceramics, organic, and carbon-based assembly[16,35–48]. Furthermore, it demonstrate that the light-matter interaction of MXene materials was effectively maximized by introducing the commercial organic ligands.

Fabrication and structural analysis of m-MXene-coated aligned LCE (m-MXene/aLCE) fibers

To demonstrate the photothermal efficacy of m-MXene for light-driven applications, fiber-type soft actuators were fabricated by simply coating the surface of LCE fibers with m-MXene sheets. Notably, LCE fibers hold significant potential as next-generation stimulus-responsive materials due to their excellent mechanical properties, programmability, large and reversible actuation, rapid shape deformation in response to various stimuli, and environmental stability[49,50]. Initially, an LCE dope solution was prepared with mesogenic acrylate species, dithiol, and quedrathiol molecules as liquid crystal molecules, chain extenders, and crosslinkers, respectively, through a thiol–acrylate click reaction (see details in Methods). Figure 3a outlines the process for fabricating LCE fibers, involving the extrusion of dope solution through hollow silicon tubes, followed by drying and winding with a bobbin. While stretching four-fold to induce alignment along the fiber axis, the LCE fibers were cured using UV light. As shown in Fig. 3b, c, the diameters of the fibers decreased during the stretching process, transforming the LCE fibers (1.12 mm) into highly aligned LCE (aLCE) fibers (0.51 mm). The 2D WAXS patterns of the LCE and aLCE fibers show that, compared to the uniform ring-shaped diffraction pattern of LCEs, the stretched samples exhibited arc-shaped and anisotropic diffraction patterns in the azimuthal angle, indicating well-aligned microstructures in the aLCE fibers.

As shown in Fig. 3d, the aLCE fibers were subsequently coated with MXene (MXene/aLCE) and OAm-MXene (m-MXene/aLCE) in water and chloroform ($CHCl_3$) phases, respectively, using a simple dip-coating method. During this process, the aLCE fibers exhibited distinct behaviors in water and $CHCl_3$. While the aLCE fibers did not undergo structural deformation during MXene coating (Fig. 3e), they experienced axial contraction and cross-sectional expansion when coated with OAm-MXene due to swelling behavior induced by the $CHCl_3$ dispersing media. Upon complete drying, the fibers reverted to their original structure, resulting in highly wrinkled surfaces, unlike the smooth and even surfaces of the MXene/aLCE fibers (Fig. 3f). In other words, the expansion following contraction along the fiber axis resulted in axis-parallel wrinkles in the m-MXene layers. The formation of wrinkled m-MXene layers without delamination is facilitated by the hydrophobic chain-chain interactions between the long alkyl chains of OAm and the LCE matrix[51,52]. For comparison, the aLCE fibers were also subjected to swelling solely in $CHCl_3$ without OAm-MXene and then dried, as shown in Supplementary Fig. 4a (s-aLCE).

The integrated 1D profiles in Fig. 3g and Supplementary Fig. 4b reveal that all samples showed peaks at the same q-value (~1.40 Å^{-1}), indicating that the intermolecular distances of LC molecules were

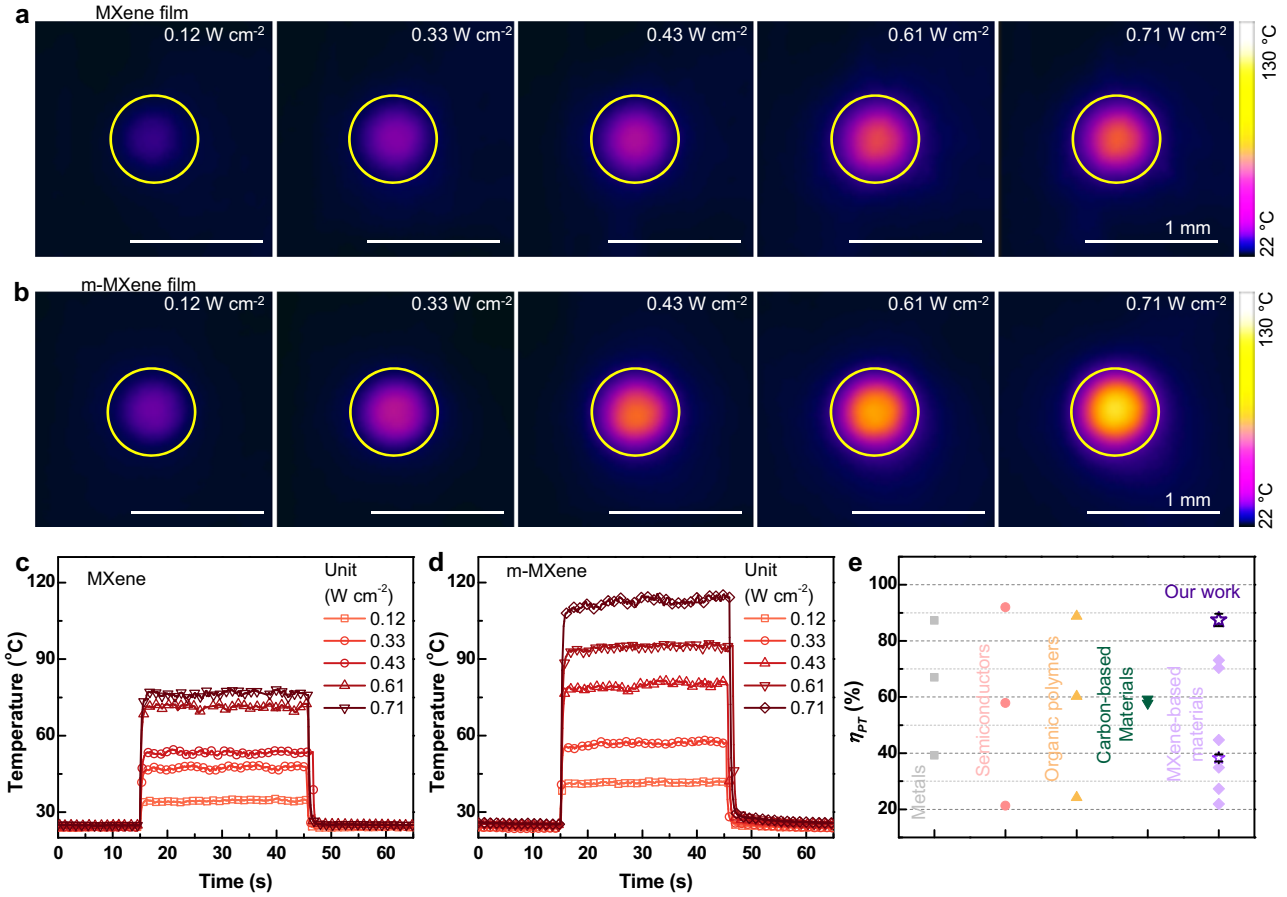

Fig. 2 | Photothermal effects and performance of m-MXene films. IR images of (**a**) MXene and (**b**) m-MXene films according to increase in light power. All scale bars are 1 mm. Surface temperature profiles of (**c**) MXene and (**d**) m-MXene film under 808 nm laser irradiation with different light power. **e** Comparison of photothermal efficiency of various photothermal materials, including metals, ceramics, organic, carbon, and MXene-based materials.

relatively consistent across all samples. However, in the azimuthal plots, while the LCE fibers showed a broad peak with an FWHM of 102.03° and f of ~0.31, the aLCE fibers exhibited a significantly narrower peak with an FWHM of 46.86°, signifying the development of a highly aligned molecular structure within the LCE fiber (f = ~0.70), which resulted from the stretching and curing processes (Fig. 3h, Supplementary Fig. 4c, and 5). The FWHM and f values of the MXene/aLCE fibers (~45.85° and ~0.71, respectively) were similar to those of the aLCEs. However, both the s-aLCE (~50.43° and ~0.66) and m-MXene/aLCE (~51.48° and 0.65) fibers showed slightly broadened peaks and a less aligned structure compared to the aLCE and MXene/aLCE fibers, indicating that the swelling behavior of LCE fibers slightly disrupts the alignment of LC molecules. Figure 3i shows the mechanical properties of the fibers. After coating with OAm-MXene, the tensile stress of the fiber increased significantly (~6.86 MPa) compared to those of aLCE (~3.35 MPa) and MXene/aLCE (~3.50 MPa) owing to the favorable interfacial interaction between the aLCE and m-MXene layers.

Figure 4a, b show the cross-sectional SEM images of the fibers, presenting a smooth thin coating layer of MXene and wrinkled layers of m-MXene. In the WAXS q plots of Fig. 3g, the m-MXene/aLCE fibers showed a peak at ~0.23 $Å^{-1}$, corresponding to the (002) peak diffraction of m-MXene layers, while no (002) peak diffraction of the MXene layers was observed in the MXene/aLCE fibers. Additionally, the scattering patterns were obtained by focusing six points on the fibers from the surface to the center with synchrotron X-ray beams (Supplementary Fig. 6a–d). Each point was spaced 50 μm apart, as schematically shown in Fig. 4c, d. The intensities of the peaks corresponding to the LC molecules (q value of 1.40 $Å^{-1}$) in fibers increased from #0 to #5 owing to the increasing thickness of fibers. The (002) peaks of the MXene layers on the MXene/aLCE fibers were observed at positions #0 to #1 but disappeared at positions #2 to #5 (Supplementary Fig. 6c). At positions #0 and #1, the MXene sheets were aligned parallel to the direction of the incident beam. As it moved toward the center of the fibers beyond position #1, the alignment of the MXene sheets deviated from the direction parallel to the beam, indicating that the MXene nanosheets were oriented along the round surface of the LCE fibers. However, the (002) peaks of the m-MXene/aLCE fibers were consistently observed at all positions because OAm-MXene sheets orientated parallel to the beam stochastically existed across all regions on the wrinkled surface of the fibers.

To numerically analyze the WAXS results at the six points, the ratios of the intensities at positions #0 to #5 are plotted in Fig. 4e. The intensity of the (002) peak of the MXene/aLCE fibers decreased to 0.71 at position #1 and eventually disappeared. By contrast, the ratio of the intensity of the m-MXene/aLCE fibers (0.86) was higher than that of MXene/aLCE fibers at position #1 and then reached saturation in the range of 0.58–0.46, indicating that the m-MXene layers have various orientations along the wrinkled surfaces of fibers. Notably, this hierarchically wrinkled surface of the m-MXene/LCE fibers caused multiple scattering of incident light, resulting in an enhanced light-to-heat conversion effect[20,21]. To investigate the impact of wrinkled surfaces on the photothermal effect, the surface temperatures generated by incident light with the same power density (1.37 W cm^{-2}) were analyzed, and the corresponding IR images at saturated surface temperature for each sample are presented in Fig. 4f, g. The m-MXene/aLCE fibers demonstrated the highest surface temperature (~105 °C) compared to

https://doi.org/10.1038/s41467-024-54802-0

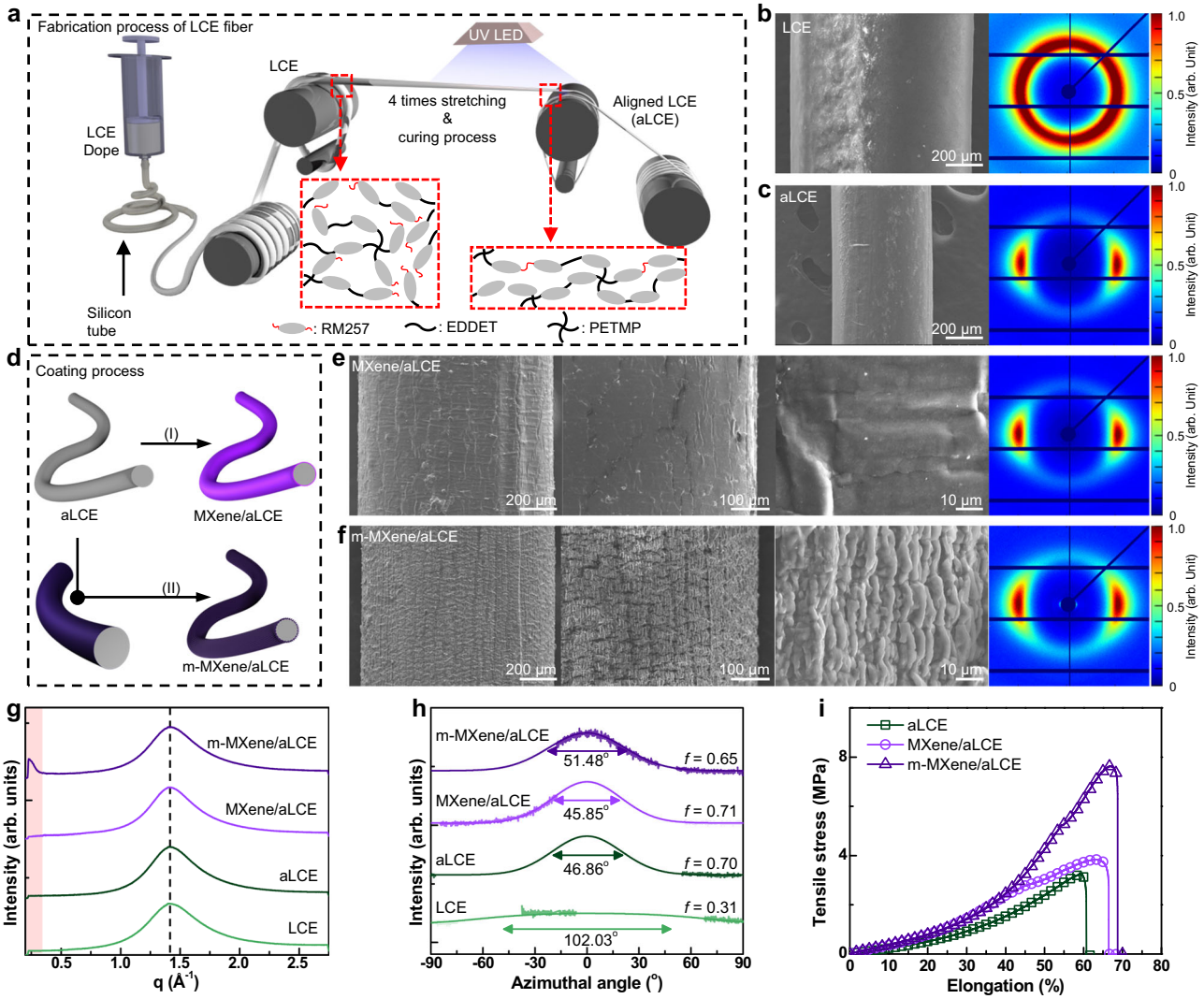

Fig. 3 | Fabrication, structural analysis, and mechanical properties of m-MXene-coated aligned LCE (m-MXene/aLCE) fibers. a Schematics showing the fabricating, stretching, and curing of LCE fibers. SEM images and 2D WAXS patterns of (**b**) LCE and (**c**) aLCE fibers. **d** Schematic of (I) MXene (lighter purple color) and (II) m-MXene (darker purple color) layer coating process on the aLCE fibers. For dip-coating the m-MXene layers on the aLCE fibers, the aLCE fibers are swollen and then recover the original structure due to the solvent ($CHCl_3$), resulting in the wrinkled m-MXene layers on the surface of aLCE fibers. SEM images and 2D WAXS patterns, respectively, of (**e**) MXene/aLCE and (**f**) m-MXene/aLCE fibers. **g** WAXS q plots and (**h**) azimuthal profiles of LCE, aLCE, MXene/aLCE, and m-MXene/aLCE fibers. **i** Tensile stress–elongation curves of aLCE, MXene/aLCE, and m-MXene/aLCE fibers. In azimuthal plots, the shading lines represent the raw data, while the solid lines indicate the smoothed data.

aLCE (~27 °C) and MXene/aLCE (~63 °C). A quantitative comparison of the temperature change ($\Delta T = T_s - T_i$) from initial (T_i) to saturated (T_s) surface temperature revealed that, while the aLCE fibers exhibited only minor changes, the ΔT of m-MXene/aLCE fibers (~80 °C) was ~2.1 times higher than that of the MXene/aLCE fibers (~38 °C). Considering that the superlattice structure of the m-MXene layers resulted in a 1.7-fold higher surface temperature than that of the MXene film (Fig. 2c, d), this additional increase in temperature highlights the enhanced light-trapping effect induced by the hierarchically wrinkled surface structure. Collectively, the photothermal performance was highly enhanced by the synergistic effect of the alternating nanostructure and hierarchically wrinkled surface microstructure.

Light-driven actuating performance and smart devices of m-MXene/aLCE fibers

As the temperature increases, the LC mesogens in the LCE transition from a nematic to an isotropic phase. This transition of the aligned LC mesogens induces macroscopic deformation, such as contraction. In this context, heat generated by photothermally effectively drives the actuation behavior of the LCE. Figure 5a shows the experimental setup used to investigate the light-driven actuating stress on the fibers. The fixed fibers were exposed to a NIR laser with a power density of 1.37 W cm^{-2}. The contractile forces of the fibers were measured as the light-driven thermal stimulus induced the phase transition of the aLCE fibers from nematic to isotropic. In Fig. 5b, no change in stress was observed in the aLCE fibers because the photothermally driven temperature change was near 0 °C. The ΔT and actuating stress of m-MXene/aLCE fibers were ~2.11- and 2.67-fold higher than those of MXene/aLCE fibers. Detailed mechanical properties, actuating stress, and ΔT are summarized in Supplementary Table 1. As the light power density increased from 0.24 to 1.38 W cm^{-2} stepwise, the surface temperature and the actuating stress of m-MXene/aLCE fibers simultaneously increased (Fig. 5c and Supplementary Fig. 7a). Furthermore, both the surface temperature and actuation strength exhibited an overall deviation of 1% during 100 repeated tests, indicating the stable actuating and photothermal performance of the aLCE network and

https://doi.org/10.1038/s41467-024-54802-0

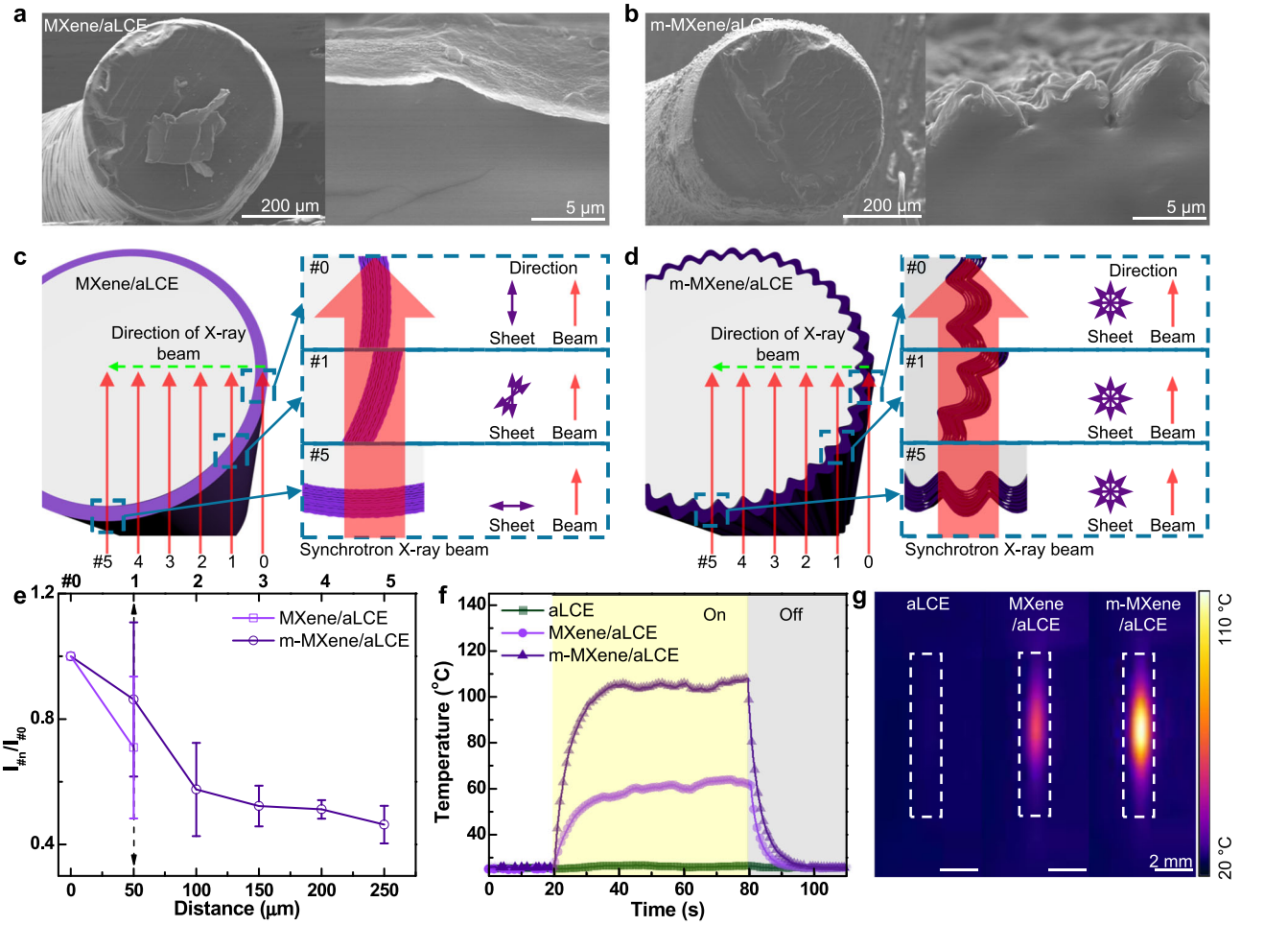

Fig. 4 | Structural analysis and photothermal effect of micro-wrinkled m-MXene/aLCE fibers. Cross-sectional and magnified SEM images of (**a**) MXene/aLCE and (**b**) m-MXene/aLCE fibers. To investigate the wrinkled surface of m-MXene/aLCE fibers, the scattering patterns are measured by focusing six points (#0, 1, 2, 3, 4, and 5) on the fibers from the surface to the center along to the green line (#0 to #5) with incident synchrotron X-ray beams (the red arrow). Each point is spaced 50 μm apart. Schematics of the difference in the surfaces of (**c**) MXene/aLCE and (**d**) m-MXene/aLCE fibers. The direction of sheet and beam mean the direction of MXene nanosheets and incident X-ray beam at each position. The MXene sheets parallel to the direction of the incident X-ray beam, are present regardless of the position due to the micro-wrinkled structure. **e** Comparison of $I_{\#n}/I_{\#0}$ ratio ($I_{\#n}$: intensity of (002) peak at #n). The error bars were given as the standard deviation ($n = 3$). **f** Surface temperature profile and (**g**) IR images of aLCE, MXene/aLCE, and m-MXene/aLCE fibers under 808 nm laser irradiation.

m-MXene layers (Fig. 5d and Supplementary Fig. 7b). To evaluate the work capacity of the m-MXene/aLCE fibers, the actuation strain was measured under various loads (0.11, 0.21, 0.42, 0.50, 0.59, and 0.67 MPa) using a 1.37 W cm^{-2} NIR source (Fig. 5e, f, and Supplementary Movie 1). The fibers exhibited actuation strains of 45.71%, 42.83%, 39.66%, 35.33%, 32.48%, and 28.83%, respectively. The m-MXene/aLCE fiber was capable of lifting ~6900 times its own weight (~2.38 mg). Although the actuation strain decreased from 45.71 to 28.83% as the load increased from 0.11 to 0.67 MPa, the work capacity continuously increased, reaching a maximum of ~228 J kg^{-1} (Fig. 5g). This work density is 6-fold higher than that of human skeletal muscle (~38 J kg^{-1})[53].

Figure 5h shows the maximum actuation strain of m-MXene/aLCE fibers over more than 1000 cycles (NIR irradiation: on for 20 s and off for 20 s) under various loads. The results demonstrate that the m-MXene/aLCE fibers maintained stable actuation. During the cycle tests, the fibers exhibited stable actuating performance without the degradation of the maximum actuation strain under all loads. The mechanical strength of the m-MXene/aLCE fibers was maintained after 1000 cycles (Supplementary Fig. 8a, b). Furthermore, Supplementary Fig. 9 represented morphological change of the m-MXene/aLCE fibers before and after cycle tests. It was observed that the crack was developed at the micro-wrinkled m-MXene layer on the aLCE surface, as applied loads increased, resulting from the extension of m-MXene/aLCE fibers in the fiber axial direction by applied loads. However, excluding the cracks, it was confirmed that the m-MXene layer is well coated on the aLCE surface. Cross-sectional SEM images revealed that both the adhesion between the aLCE and m-MXene layer and the micro-wrinkled structures of the m-MXene layer are also maintained stably. It confirms the adhesion and structural stability of wrinkled m-MXene layer, and the stability of the light-driven actuation of the m-MXene/aLCE fibers.

The mechanical and photothermal stability of the m-MXene/aLCE fibers were further investigated under environmental conditions of 60 °C and 99.9% R.H. for 33 days. When irradiated with a NIR laser (1.25 W cm^{-2}), the surface temperature of the m-MXene/aLCE fibers initially reached ~100 °C. After 33 days in these conditions, the surface temperature showed ~107 °C (Supplementary Fig. 10a–c). Throughout the environmental stability test, the mechanical strength of the m-MXene/aLCE fibers remained stable, showing no degradation, and maintained a strength of ~6.32 MPa after 33 days under the same conditions (Supplementary Fig. 11a, b). These results clearly demonstrate the excellent environmental stability of the m-MXene/aLCE

https://doi.org/10.1038/s41467-024-54802-0

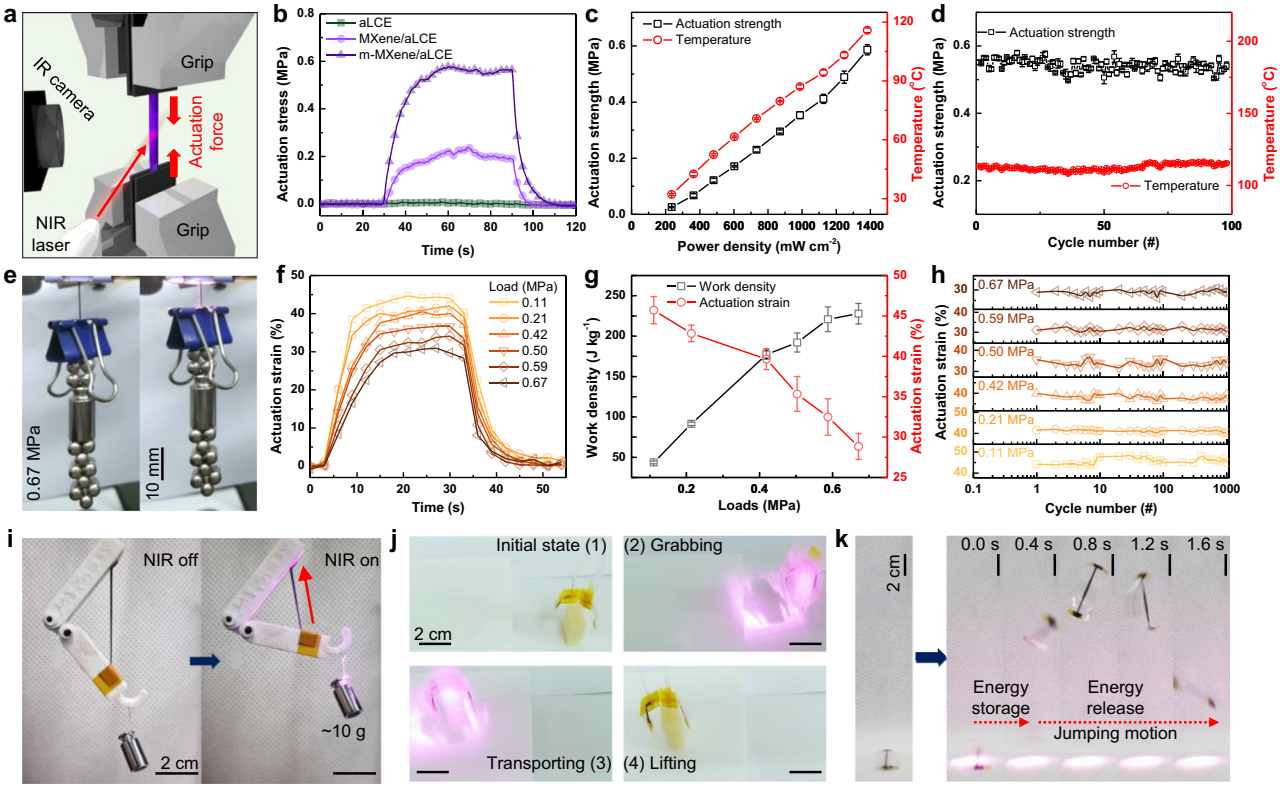

Fig. 5 | Light-driven actuating performance of m-MXene/aLCE fibers. **a** Schematic demonstrating the setup of actuating stress measurement. The m-MXene/aLCE fiber is loaded with the zig of UTM to measure the actuation force and IR camera to obtain the surface temperature photothermally generated. Under NIR irradiation, the temperature of m-MXene/aLCE fiber increases and results in actuation force (contraction). **b** Actuation stress profile of aLCE, MXene/aLCE, and m-MXene/aLCE fibers. **c** Actuation strength and temperature plots according to power density of irradiated NIR laser. The error bars are given as the standard deviation ($n = 3$). **d** Cycle test of m-MXene/aLCE fibers. The error bars are given as the standard deviation ($n = 6$). **e** Lifting test of an m-MXene/aLCE fiber under a load of 0.67 MPa. **f** Actuation strain profile, **g** maximum actuation strain and work capacity. The error bars are given as the standard deviation ($n = 28$), and **h** stability test for more than 1000 cycles at applied loads of 0.11, 0.21, 0.42, 0.50, 0.59, and 0.67 MPa by NIR laser of 1.37 W cm^{-2}. **i** Artificial biceps model, **j** gripper application and **k** jumping film using curved 2D PET film (curvature = 20 m^{-1}) of m-MXene/aLCE fibers.

fibers, highlighting their improved mechanical properties and photothermal performance. As shown in Supplementary Fig. 12, the m-MXene/aLCE fibers showed outstanding actuation strength and considerable actuation strain compared to LCE actuators, including LCE materials, electronic wire embedded LCE, vascular structured LCE, and functional material coated LCE[54–64].

By mimicking the human bicep muscle, the three strands of fibers in an arm model device successfully lifted a 10 g weight reversibly (Fig. 5i and Supplementary Movie 2). A simple gripper was fabricated using a polyethylene terephthalate (PET) substrate with m-MXene/aLCE fibers as the actuating component. The gripper effectively grasped a cubic object upon exposure to the NIR laser and released it immediately after turning the light off (Fig. 5j and Supplementary Movie 3: grasp ((1)–(2)), transfer ((2)–(3)), and lift ((3)–(4)). Furthermore, by introducing a structural design (e.g., a bistable structure), the energy generated by the soft actuator was stored and rapidly released[65]. The m-MXene/aLCE fibers were also employed on the surface of a compliant PET structure with a curvature of 20 m^{-1} to prepare a bistable jumping film, as shown in Fig. 5k and Supplementary Movie 4. The film demonstrated a jumping height of ~17.8 cm within 0.8 s. The photothermally driven contraction force of the actuators fixed at the curved edge deformed the flat shell into a concave state, resulting in snapping and jumping behavior.

The bistable devices were prepared by designing a beam-column model with flexible PET beam linkers and a rigid polylactic acid (PLA) column (Fig. 6a). In Fig. 6b, the typical force–displacement relationship is illustrated. Applying a force greater than the critical force to a column in the first stable state (black dotted line) caused the column to move to the snap-through point (red dotted line). Subsequently, through the snapping motion, the column transitioned to a second stable state (blue dotted line). The bistable device exhibited a critical force of ~0.57 N and a snap-through point of 7.95 mm, indicating that to actuate this bistable device, an applied force, and displacement exceeding 0.57 N and 7.95 mm, respectively, was required (Fig. 6c). Considering the actuating force and strain of the m-MXene/aLCE fibers, two bundles of six strands of fibers were integrated on both sides of the bistable device (Fig. 6d and Supplementary Movie 5), and a simple shooting device was designed, as shown in Fig. 6e (Supplementary Movie 6). The elastic instability of the bistable device rapidly stored and released energy, which was photothermally generated. This high-speed locomotion facilitated shooting. Furthermore, a mechanical gripper was developed to enable grabbing and releasing motions through an up-and-down motion. A bistable actuator was coupled to the gripper as a driving device to create a switchable gripper (Fig. 6f). This switchable gripper demonstrated a deforming motion between stable and distinct bi-states (grabbing and releasing states) in Supplementary Movie 7. Notably, it maintained the grabbing or releasing motion without the incident NIR laser, highlighting an energy-efficient approach for motion

https://doi.org/10.1038/s41467-024-54802-0

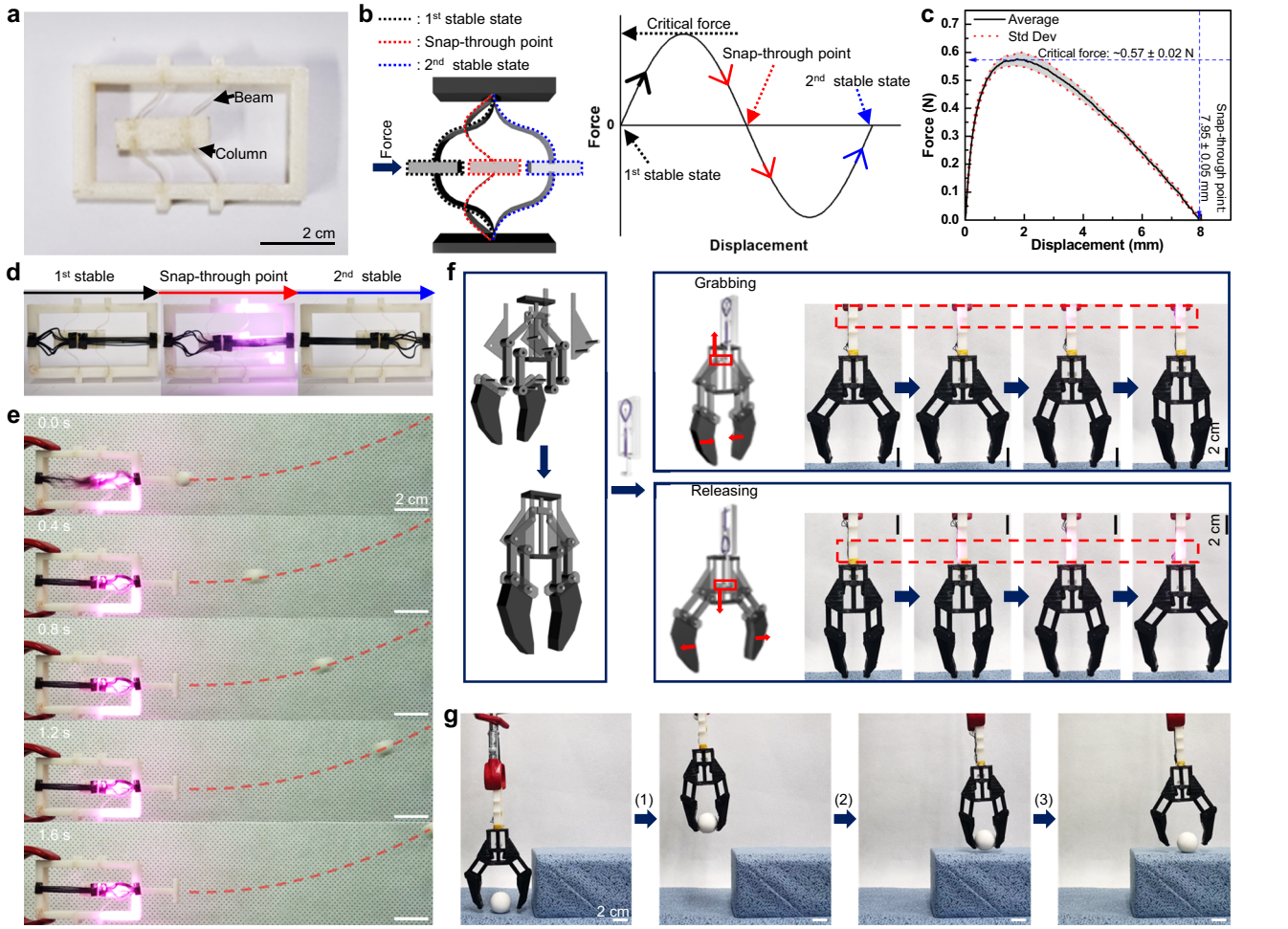

Fig. 6 | Smart and soft devices of m-MXene/aLCE fibers. a Optical image and (**b**) schematic demonstration of the bistable device (beam–column model) and typical curve of force and displacement relationship. **c** Force–displacement curve of the fabricated bistable device. The error bars are given as the standard deviation ($n = 5$). **d** Optical images of a bistable actuator fabricated by integrating two bundles of six strands of m-MXene/aLCE fibers from 1st to 2nd stable state. **e** Shooting motion of a bistable actuator. **f** Schematic of assembling a switchable gripper and demonstrating photothermal grabbing and releasing motion of a switchable gripper. **g** Application of a switchable gripper: (1) lifting, (2) transporting, and (3) releasing.

maintenance. Eventually, the switchable gripper functioned effectively and stably in grabbing (1), transferring (2), and releasing (3) a spherical object (Fig. 6g and Supplementary Movie 8). Thus, the exceptional photothermal efficiency of m-MXene is attributed to the formation of a superlattice structure incorporating organic layers with low RI and MXene nanosheets. This unique structure allows m-MXene to exhibit outstanding photothermal efficiency. The resulting light-driven actuating fibers, which feature a micropatterned surface that enhances the photothermal effect on the surface, can be easily produced and applied as efficient switchable actuators.

Discussion

In summary, MXene-based metamaterials (m-MXene) were developed to exhibit enhanced light absorption behavior by assembling MXene nanosheets with organic functional groups featuring low RI values into densely packed alternating layered structures. The self-assembled superlattice structure of the m-MXene films increased light absorption through a low RI and multiple reflections within the structures. Compared to MXene films, the m-MXene films exhibited more than a two-fold decrease in reflection, eventually achieving a photothermal conversion efficiency of up to 90%, surpassing that of the MXene films by 2.3 times (~38%). Coating m-MXene onto LCE fibers induced significant wrinkling of the fiber surface owing to swelling and contraction during the coating process. These micro-wrinkled surfaces of the m-MXene layers on LCE fibers facilitated light trapping, further enhancing the photothermal conversion. The integration of these fibers into photothermally driven actuator devices, which demonstrated outstanding durability and lift capability, highlights the versatility of our approach. It should be noted that comparative photothermal properties were obtained by designing nonarchitectures of the MXene and organic layers.

Methods

Materials

Ti_3AlC_2 MAX-phase powders (particle size <200 µm, Ukraine) were obtained from Carbon-Ukraine Ltd. 35% hydrochloric acid (HCl) solution, 99.995% lithium fluoride (LiF) powder, pentaerythritol tetrakis(3-mercaptopropionate) (PETMP), 2,2-(ethylenedioxy) diethanethiol (EDDET), 2-Hydroxy-4′-(2-hydroxyethoxy)−2-methylpropiophenone, and dipropylamine (DPA) toluene were purchased from Sigma-Aldrich Co. (St. Louis, MO). 4-bis-[4-(3-acryloyloxypropypropyloxy) benzoyloxy]-2-methylbenzene (RM257) was purchased from ChemScene. Oleylamine was obtained from Cejin CI Co. (Seoul, Korea). Deionized water was obtained using a water-purification system (Direct Q3) purchased from Millipore (Bedford, MA).

Synthesis of delaminated $Ti_3C_2T_x$ MXene and oleylamine modified MXene (OAm-MXene)

$Ti_3C_2T_x$ MXene was synthesized by etching the Al layer of the Ti_3AlC_2 MAX phase[23]. 1 g of LiF was dissolved in 20 mL of a 9 M HCl solution for 30 min at 35 °C using a perfluoroalkoxy alkane flask. 1 g Ti_3AlC_2 powder was carefully added and stirred for 24 h. After the etching reaction, excess acid was removed via centrifugation at 1507 RCF for 5 min until the pH reached ~6. Next, the delaminated $Ti_3C_2T_x$ MXene nanosheets were obtained by centrifugation at 651 RCF for 1 h. The obtained aqueous MXene dispersion was diluted to 0.1 wt% MXene nanosheets were modified by organic molecules (i.e., oleylamine) according to our previously reported method[23]. The oleylamine (OAm) was dissolved in chloroform at a ratio of 0.5 mmol of oleylamine per gram of MXene. Subsequently, the MXene dispersion was carefully poured into the oleylamine solution and then vigorously stirred for 24 h at room temperature. The OAm-MXene transferred in chloroform was obtained by removing the transparent aqueous phase. Centrifugation at 7871 RCF for 5 min was performed to remove the unreacted oleylamine and concentrate the OAm-MXene dispersion. A 5 mg mL^{-1} OAm-MXene dispersion was prepared.

Characterization

FT-IR spectroscopy was performed using a Nicolet iS50 spectrometer (Thermo Fisher Scientific) using the attenuated total reflection technique. XPS was performed using a Theta probe (Thermo Fisher Scientific) with monochromatic Al Kα radiation. UV–vis spectroscopy was performed using a Lambda 650s (PerkinElmer). The specific heats of the MXene and m-MXene films were measured by differential scanning calorimetry (DSC) using DSC 21 Polyma. These measurements were performed using instruments installed at the Hanyang LINC3.0 Analytical Equipment Center (Seoul). SEM images were obtained using an S-4800 microscope (Hitachi) at 15 kV and 10 μA without Pt sputtering. For cross-sectional images, Pt sputtering was conducted. Spectroscopic ellipsometry was performed using an Alpha-SE® ellipsometer (J.A. Woolam Co. Inc.) at Kyun Hee University. For the ellipsometry analysis, MXene and m-MXene were spin-coated onto polished silicon wafers. All measurements were performed at a fixed angle of incidence in the wavelength range of 380 to 890 nm. Synchrotron WAXS measurements were performed at the 4C SAXS II beamline of the Pohang Accelerator Laboratory (Pohang, Republic of Korea) with an X-ray beam wavelength of 0.675 Å and sample-to-detector distance of 20 cm[25]. The MXene and m-MXene films were given an exposure time of 10 s, and those of the LCE, MXene, and m-MXene/aLCE fibers were 30 s. Additional WAXS data were measured while moving the loaded fiber at 50 μm intervals. A NIR laser was generated using fiber-coupled MDL-I-808 for photothermal applications. The tensile properties of the LCE, MXene, and m-MXene/aLCE fibers were investigated using a universal testing machine (5966, Instron, USA) equipped with a 10-N load cell operating at a 1 mm min^{-1} crosshead speed and gauge length of 10 mm. The force–displacement of the bistable device was also measured using the UTM equipment. The fibers were then loaded onto a rectangular frame. The mechanical strength of the fibers was calculated by dividing the force by the cross-sectional area. IR thermal image and temperature profiles were acquired using an A320 thermal imaging camera (FLIR Systems) at temperatures below 250 °C. For accuracy of mechanical properties, photothermal effect, and actuation properties, those measurements were repeated more than three times. The characterizations were conducted at room temperature. All schematic illustrations were designed by 3Ds Max.

Fabrication of LCE, MXene, and m-MXene/aLCE fibers

The LCE dope was obtained following a previous study[61]. RM257 (1.19 g, 2.00 mmol) was dissolved in 0.3 mL of toluene at 80 °C. EDDET (0.28 g, 1.50 mmol), PETMP (0.07 g, 0.14 mmol), and 2-Hydroxy-4′-(2-hydroxyethoxy)−2-methylpropiophenone (7 mg) were added in the solution. DPA was diluted in toluene at a mass ratio of 1:50, and the diluted DPA solution (293 mg) was mixed and vigorously stirred in the prepared solution. The solution was degassed in a vacuum oven and transferred to a syringe. The LCE dope was injected into a silicon tube that served as a mold. After 12 h, the fabricated LCE was finally put into an 80 °C oven for 12 h. The LCE fibers were continuously stretched to four times their original length and cured using a homemade drawing machine under UV light (365 nm). The MXene/aLCE was fabricated by dip coating the aLCE fiber with O_2 plasma treatment for 1 min. By contrast, the m-MXene/aLCE fibers were obtained by dip coating the aLCE fibers without plasma treatment, and the coated fibers were dried for 24 h in an ambient environment. For environmental stability tests, the m-MXene/aLCE fibers were exposed to harsh condition (60 °C and 100% R.H.) in oven.

Preparation of a bistable device and switchable gripper

The support and column of the bistable device were printed using a 3D printer (FlashForge) and PLA filaments in PolyMaker. The beams were fabricated using PET with a width of 5 mm. Four beams with a length of ~11.5 mm were connected between the support and column with a spacing of 10 mm. A suitable actuator was fabricated by combining m-MXene/aLCE fibers with the device. A gripper printed in FlashForge by PLA was assembled, and a switchable gripper was obtained by integrating the as-prepared bistable actuator with the gripper.

Determination of the degree of orientation in fibers

Herman's orientation function (f) is defined as follows[26]:

$$f = \frac{1}{2}3\langle\cos^2\theta\rangle - 1 \tag{1}$$

$$\langle\cos^2\theta\rangle = \frac{\int_0^{\pi/2} I(\theta)\cos^2\theta \sin\theta d\theta}{\int_0^{\pi/2} I(\theta)\sin\theta d\theta} \tag{2}$$

where $I(\theta)$ is the intensity at θ in the azimuthal plots, obtained from the WAXS data (Figs. 1d, 3h, and Supplementary Fig. 4c).

Calculation of photothermal conversion efficiency

The photothermal conversion efficiency (η_{PT}) was calculated following two equations[34] according to the equation at a fixed power (0.71 W cm^{-2}).

$$\eta_{PT} = hA\triangle T_{max}/I \tag{3}$$

where h, A, ΔT_{max}, and I represent the heat transfer coefficient, surface area of the system, the temperature difference between the maximum steady-state temperature and ambient temperature, and light power, respectively. Using θ defined as the ratio of ΔT to ΔT_{max}, hA is calculated according to

$$t = -\frac{\sum_i m_i C_{p,i}}{hA}\ln\theta \tag{4}$$

Therefore, through the linear relationship of time data from the cooling period t with $-\ln\theta$, the hA was derived. The specific heat (C_p) of the MXene and m-MXene films was measured using DSC. Introducing the hA value into Eq. (3), the photothermal conversion efficiency (η_{PT}) was obtained.

Data availability

All data generated in this study are provided in the article, Supplementary Information, and Source Data file. All data are available from the corresponding author upon request. Source data are provided with this paper.

References

1. Cui, X. et al. Photothermal nanomaterials: a powerful light-to-heat converter. *Chem. Rev.* **123**, 6891–6952 (2023).
2. Kim, H. J., Kim, B., Auh, Y. & Kim, E. Conjugated organic photothermal films for spatiotemporal thermal engineering. *Adv. Mater.* **33**, 2005940 (2021).
3. Han, B., Zhang, Y. L., Chen, Q. D. & Sun, H. B. Carbon-based photothermal actuators. *Adv. Funct. Mater.* **28**, 1802235 (2018).
4. Huang, J., Zhao, L., Wang, T., Sun, W. & Tong, Z. NIR-triggered rapid shape memory PAM–GO–gelatin hydrogels with high mechanical strength. *ACS Appl. Mater. Interfaces* **8**, 12384–12392 (2016).
5. Xie, Z. et al. The rise of 2D photothermal materials beyond graphene for clean water production. *Adv. Sci.* **7**, 1902236 (2020).
6. Xu, D., Li, Z., Li, L. & Wang, J. Insights into the photothermal conversion of 2D MXene nanomaterials: synthesis, mechanism, and applications. *Adv. Funct. Mater.* **30**, 2000712 (2020).
7. Tee, S. Y. et al. Advances in photothermal nanomaterials for biomedical, environmental and energy applications. *Nanoscale* **13**, 14268–14286 (2021).
8. Li, R., Zhang, L., Shi, L. & Wang, P. MXene Ti_3C_2: an effective 2D light-to-heat conversion material. *ACS Nano* **11**, 3752–3759 (2017).
9. Li, Y. et al. 2D $Ti_3C_2T_x$ MXenes: visible black but infrared white materials. *Adv. Mater.* **33**, 2103054 (2021).
10. Zheng, Z., Liu, H., Wu, D. & Wang, X. Polyimide/MXene hybrid aerogel-based phase-change composites for solar-driven seawater desalination. *Chem. Eng. J.* **440**, 135862 (2022).
11. Xing, C. et al. Two-dimensional MXene (Ti_3C_2)-integrated cellulose hydrogels: toward smart three-dimensional network nanoplatforms exhibiting light-induced swelling and bimodal photothermal/chemotherapy anticancer activity. *ACS Appl. Mater. Interfaces* **10**, 27631–27643 (2018).
12. Fan, X. et al. MXene $Ti_3C_2T_x$ for phase change composite with superior photothermal storage capability. *J. Mater. Chem. A* **7**, 14319–14327 (2019).
13. Zhao, J. et al. A hydrophobic surface enabled salt-blocking 2D Ti_3C_2 MXene membrane for efficient and stable solar desalination. *J. Mater. Chem. A* **6**, 16196–16204 (2018).
14. Dai, C. et al. Biocompatible 2D titanium carbide (MXenes) composite nanosheets for pH-responsive MRI-guided tumor hyperthermia. *Chem. Mater.* **29**, 8637–8652 (2017).
15. Fan, X., Ding, Y., Liu, Y., Liang, J. & Chen, Y. Plasmonic $Ti_3C_2T_x$ MXene enables highly efficient photothermal conversion for healable and transparent wearable device. *ACS Nano* **13**, 8124–8134 (2019).
16. Zhang, D. et al. Boosting the photothermal conversion efficiency of MXene film by porous wood for light-driven soft actuators. *Chem. Eng. J.* **450**, 138013 (2022).
17. Yang, Z. P., Ci, L., Bur, J. A., Lin, S. Y. & Ajayan, P. M. Experimental observation of an extremely dark material made by a low-density nanotube array. *Nano Lett.* **8**, 446–451 (2008).
18. Berdiyorov, G. Optical properties of functionalized $Ti_3C_2T_2$ (T=F, O, OH) MXene: first-principles calculations. *AIP Adv.* **6**, 055105 (2016).
19. Ren, H. et al. Hierarchical graphene foam for efficient omnidirectional solar–thermal energy conversion. *Adv. Mater.* **29**, 1702590 (2017).
20. Tao, P. et al. Bioinspired engineering of thermal materials. *Adv. Mater.* **27**, 428–463 (2015).
21. Wang, X., Liu, Q., Wu, S., Xu, B. & Xu, H. Multilayer polypyrrole nanosheets with self-organized surface structures for flexible and efficient solar–thermal energy conversion. *Adv. Mater.* **31**, 1807716 (2019).
22. Wang, P. et al. Molecular plasmonics with metamaterials. *Chem. Rev.* **122**, 15031–15081 (2022).
23. Shin, H., Lee, H., Seo, Y., Jeong, W. & Han, T. H. Grafting behavior of amine ligands for surface modification of MXene. *Langmuir* **39**, 2358–2367 (2023).
24. Maleski, K., Shuck, C. E., Fafarman, A. T. & Gogotsi, Y. The broad chromatic range of two-dimensional transition metal carbides. *Adv. Opt. Mater.* **9**, 2001563 (2021).
25. Kim, K. W. et al. Small-angle X-ray scattering beamline BL4C SAXS at Pohang light source II. *Biodesign* **5**, 24–29 (2017).
26. Park, H. et al. Dynamic assembly of liquid crystalline graphene oxide gel fibers for ion transport. *Sci. adv.* **4**, eaau2104 (2018).
27. Ghobadi, A., Hajian, H., Butun, B. & Ozbay, E. Strong light–matter interaction in lithography-free planar metamaterial perfect absorbers. *ACS Photonics* **5**, 4203–4221 (2018).
28. Han, J., Lin, K. T., Lin, H., Lau, K. T. & Jia, B. Tunable thermochromic graphene metamaterials with iridescent color. *Nano Lett.* **22**, 6026–6033 (2022).
29. Jin, Y. et al. A highly flexible and washable nonwoven photothermal cloth for efficient and practical solar steam generation. *J. Mater. Chem. A* **6**, 7942–7949 (2018).
30. Huang, Y. et al. Hybrid superlattices of two-dimensional materials and organics. *Chem. Soc. Rev.* **49**, 6866–6883 (2020).
31. Li, K. et al. Biomimetic MXene textures with enhanced light-to-heat conversion for solar steam generation and wearable thermal management. *Adv. Energy Mater.* **9**, 1901687 (2019).
32. Shahzad, F. et al. Electromagnetic interference shielding with 2D transition metal carbides (MXenes). *Science* **353**, 1137–1140 (2016).
33. Li, B., Luo, S., Anwer, S., Chan, V. & Liao, K. Heterogeneous films assembled from $Ti_3C_2T_x$ MXene and porous double-layered carbon nanosheets for high-performance electromagnetic interference shielding. *Appl. Surf. Sci.* **599**, 153944 (2022).
34. Cao, Y. et al. Highly efficient NIR-II photothermal conversion based on an organic conjugated polymer. *Chem. Mater.* **29**, 718–725 (2017).
35. Chang, L. et al. Carbon-doped γ-Ti_3O_5 film with enhanced photothermal conversion performance. *Vacuum* **212**, 111985 (2023).
36. Yu, J., Zhu, D., Qi, C. & Zhang, W. Study on the evaporation characteristics of Ag@ Fe_3O_4 nanoparticle film interface. *Sol. Energy* **258**, 16–27 (2023).
37. Qin, Y. et al. Dyeable PAN/CuS nanofiber membranes with excellent mechanical and photothermal conversion properties via electrospinning. *ACS Appl. Polym. Mater.* **4**, 9144–9150 (2022).
38. Hsiao, Y.-C. et al. Photothermal-irradiated polyethyleneimine–polypyrrole nanopigment film-coated polyethylene fabrics for Infrared-Inspired with pathogenic evaluation. *ACS Appl. Mater. Interfaces* **13**, 2483–2495 (2021).
39. Zhao, Y. et al. Photonically-activated molecular excitations for thermal energy conversion in porphyrinic compounds. *J. Phys. Chem. C.* **124**, 1575–1584 (2019).
40. Xu, K. et al. Near-infrared light-triggered multi-mode synergetic therapy for improving antibacterial and osteogenic activity of titanium implants. *Appl. Mater. Today* **24**, 101155 (2021).
41. Sun, Q. et al. Graphene nanoplatelets/Eucommia rubber composite film with high photothermal conversion performance for soil mulching. *J. Taiwan Inst. Chem. Eng.* **111**, 239–245 (2020).
42. Meng, D. et al. The enhanced photothermal effect of graphene/conjugated polymer composites: photoinduced energy transfer and applications in photocontrolled switches. *Chem. Commun.* **50**, 14345–14348 (2014).
43. Yang, H. et al. Developed carbon nanotubes/gutta percha nanocomposite films with high stretchability and photo-thermal conversion efficiency. *J. Mater. Res. Technol.* **9**, 8884–8895 (2020).
44. Liu, Y., Lin, Z., Wang, P., Huang, F. & Sun, J.-L. Measurement of the photothermal conversion efficiency of CNT films utilizing a Raman spectrum. *Nanomater* **12**, 1101 (2022).

45. Ma, X. et al. Degradable $Ti_3C_2T_x$ MXene nanosheets containing a lignin polyurethane photothermal foam (LPUF) for rapid crude oil cleanup. *ACS Appl. Nano Mater.* **5**, 2848–2858 (2022).
46. Yang, D. et al. Flexible transparent polypyrrole-decorated MXene-based film with excellent photothermal energy conversion performance. *ACS Appl. Mater. Interfaces* **13**, 8909–8918 (2021).
47. Xiang, Z., Shi, Y., Zhu, X., Cai, L. & Lu, W. Flexible and waterproof 2D/1D/0D construction of MXene-based nanocomposites for electromagnetic wave absorption, EMI shielding, and photothermal conversion. *Nano-Micro Lett.* **13**, 150 (2021).
48. Cao, W.-T. et al. Two-dimensional MXene-reinforced robust surface superhydrophobicity with self-cleaning and photothermal-actuating binary effects. *Mater. Horiz.* **6**, 1057–1065 (2019).
49. Jiang, H., Li, C. & Huang, X. Actuators based on liquid crystalline elastomer materials. *Nanoscale* **5**, 5225–5240 (2013).
50. Xiong, J., Chen, J. & Lee, P. S. Functional fibers and fabrics for soft robotics, wearables, and human–robot interface. *Adv. Mater.* **33**, 2002640 (2021).
51. Wang, L. et al. Lotus leaf inspired superhydrophobic rubber composites for temperature stable piezoresistive sensors with ultrahigh compressibility and linear working range. *Chem. Eng. J.* **405**, 127025 (2021).
52. Yu, Y. et al. Light-driven core-shell fiber actuator based on carbon nanotubes/liquid crystal elastomer for artificial muscle and phototropic locomotion. *Carbon* **187**, 97–107 (2022).
53. Madden, J. D. et al. Artificial muscle technology: physical principles and naval prospects. *IEEE J. Ocean. Eng.* **29**, 706–728 (2004).
54. He, Q. et al. Electrically controlled liquid crystal elastomer–based soft tubular actuator with multimodal actuation. *Sci. Adv.* **5**, eaax5746 (2019).
55. He, Q. et al. Electrospun liquid crystal elastomer microfiber actuator. *Sci. Robot.* **6**, eabi9704 (2021).
56. Thomsen, D. L. et al. Liquid crystal elastomers with mechanical properties of a muscle. *Macromolecules* **34**, 5868–5875 (2001).
57. Wang, M. et al. A liquid crystal elastomer-based unprecedented two-way shape-memory aerogel. *Adv. Sci.* **8**, 2102674 (2021).
58. Cho, E.-H., Luu, K. & Park, S.-Y. Mechano-actuated light-responsive main-chain liquid crystal elastomers. *Macromolecules* **54**, 5397–5409 (2021).
59. Roach, D. J. et al. Long liquid crystal elastomer fibers with large reversible actuation strains for smart textiles and artificial muscles. *ACS Appl. Mater. Interfaces* **11**, 19514–19521 (2019).
60. Sánchez-Ferrer, A. et al. Photo-crosslinked side-chain liquid-crystalline elastomers for microsystems. *Macromol. Chem. Phys.* **210**, 1671–1677 (2009).
61. He, Q., Wang, Z., Song, Z. & Cai, S. Bioinspired design of vascular artificial muscle. *Adv. Mater. Technol.* **4**, 1800244 (2019).
62. Wang, Y., Wang, Z., He, Q., Iyer, P. & Cai, S. Electrically controlled soft actuators with multiple and reprogrammable actuation modes. *Adv. Intel. Syst.* **2**, 1900177 (2020).
63. Liu, H. et al. An electrically actuated soft artificial muscle based on a high-performance flexible electrothermal film and liquid-crystal elastomer. *ACS Appl. Mater. Interfaces* **12**, 56338–56349 (2020).
64. Xiao, Y. Y., Jiang, Z. C., Tong, X. & Zhao, Y. Biomimetic locomotion of electrically powered "Janus" soft robots using a liquid crystal polymer. *Adv. Mater.* **31**, 1903452 (2019).
65. Chi, Y. et al. Bistable and multistable actuators for soft robots: structures, materials, and functionalities. *Adv. Mater.* **34**, 2110384 (2022).

Acknowledgements

We thank the Nano & Material Technology Development Program (RS-2024-00408845 and 2022M3H4A1A03085360) of the National Research Foundation of Korea funded by Ministry of Science, ICT & Future Planning of Korea. This work was also supported by U.S. Army Combat Capabilities Development Command Soldier Center (DEVCOM SC) and U.S. Army International Technology Center Pacific (FA5209-23-C0029 and FA5209-22-P0199). The prepared samples were analyzed by spectroscopy at the Hanyang LINC Analytical Equipment Center (Seoul). Experiments at Pohang Accelerator Laboratory (PAL 4C) were supported in part by the Ministry of Science, ICT, and Future Planning of Korea.

Author contributions

Conceptualization and supervision, T.H.H.; methodology, investigation, and data analysis, H.S.; data measurement, H.S. and W.J.

Competing interests

The authors declare no competing interests.

Additional information

Supplementary information The online version contains supplementary material available at https://doi.org/10.1038/s41467-024-54802-0.

Correspondence and requests for materials should be addressed to Tae Hee Han.

Peer review information *Nature Communications* thanks Xianhu Liu, Baisheng Sa and the other, anonymous, reviewer(s) for their contribution to the peer review of this work. A peer review file is available.